

ULRR

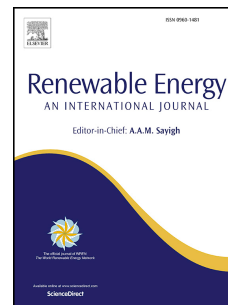
Efficient production of 5-ethoxymethylfurfural from 5-hydroxymethylfurfural and carbohydrates over lewis/brønsted hybrid magnetic dendritic fibrous silica core-shell catalyst

Item Type	Article
Authors	Hafizi, Hamid;Walker, Gavin;Collins, Maurice
Citation	Renewable Energy;183, pp. 459-471
Publisher	Elsevier
Download date	2026-04-12 13:22:25
Item License	https://creativecommons.org/licenses/by-nc-sa/1.0/
Link to Item	https://hdl.handle.net/10344/10832

Journal Pre-proof

Efficient production of 5-ethoxymethylfurfural from 5-hydroxymethylfurfural and carbohydrates over lewis/brønsted hybrid magnetic dendritic fibrous silica core-shell catalyst

Hamid Hafizi, Gavin Walker, Maurice N. Collins



PII: S0960-1481(21)01605-0

DOI: <https://doi.org/10.1016/j.renene.2021.11.036>

Reference: RENE 16208

To appear in: *Renewable Energy*

Received Date: 12 July 2021

Revised Date: 15 October 2021

Accepted Date: 7 November 2021

Please cite this article as: Hafizi H, Walker G, Collins MN, Efficient production of 5-ethoxymethylfurfural from 5-hydroxymethylfurfural and carbohydrates over lewis/brønsted hybrid magnetic dendritic fibrous silica core-shell catalyst, *Renewable Energy* (2021), doi: <https://doi.org/10.1016/j.renene.2021.11.036>.

This is a PDF file of an article that has undergone enhancements after acceptance, such as the addition of a cover page and metadata, and formatting for readability, but it is not yet the definitive version of record. This version will undergo additional copyediting, typesetting and review before it is published in its final form, but we are providing this version to give early visibility of the article. Please note that, during the production process, errors may be discovered which could affect the content, and all legal disclaimers that apply to the journal pertain.

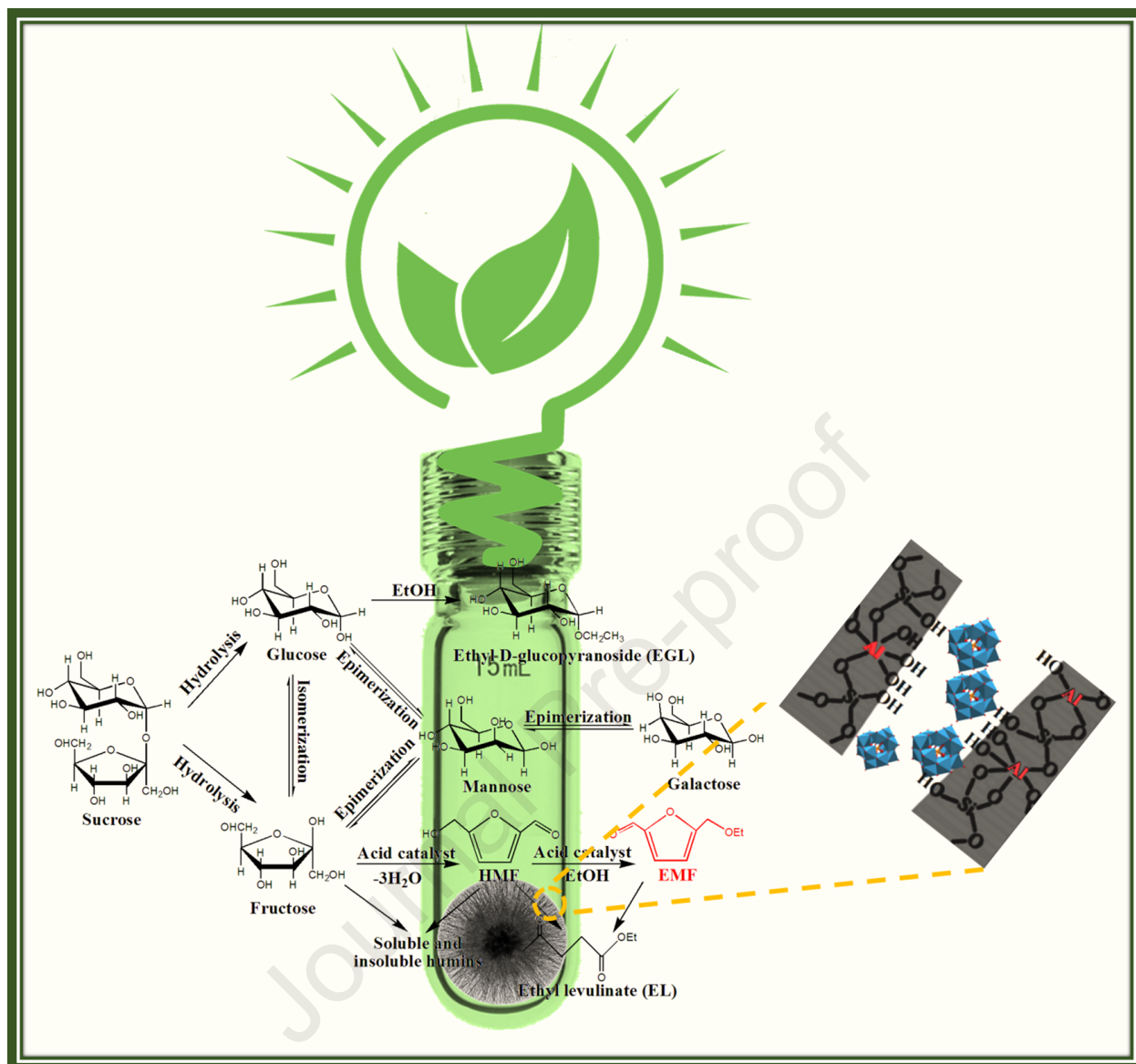
© 2021 Published by Elsevier Ltd.

H.H. Conceptualization: methodology; formal analysis; Data Curation; Writing – Original draft; Writing -Review and editing

G.W. Supervision; project administration; Resources

M.N.C. Supervision; project administration; Resources; Writing – Original draft; Writing - Review and editing

Journal Pre-proof



1 **Efficient production of 5-ethoxymethylfurfural from 5-hydroxymethylfurfural and**
2 **carbohydrates over Lewis/Brønsted hybrid magnetic dendritic fibrous silica core-shell**
3 **catalyst**

4 Hamid Hafizi^a, Gavin Walker^a, Maurice N. Collins^{b*}

5
6 ^a Department of Chemical and Environmental Sciences, Bernal Institute, University of
7 Limerick, Limerick, Ireland

8 ^b School of Engineering, Stokes Laboratories, Bernal Institute, University of Limerick,
9 V94T9PX Limerick, Ireland

10 * Corresponding author, E-mail: maurice.collins@ul.ie.

11

12

13

14

15

16

17

18

19

20

21

22

23

24 Abstract

25 In the present work, a series of Brønsted and Lewis hybrid, magnetic, dendritic fibrous silica
26 microsphere core shell particles with an open and easily accessible mesopore channels as the
27 catalyst supports ($\text{Fe}_3\text{O}_4@\text{SiO}_2@\text{KCC-1}$) were prepared, impregnated with aluminum (10
28 wt%) followed by encapsulation of different loadings of tungstophosphoric acid (PTA) from
29 10 to 40 wt% into mesoporous channels of fibrous silica shell ($\text{Fe}_3\text{O}_4@\text{SiO}_2@\text{KCC-}$
30 $1/\text{Al}_{10}/\text{PTA}_x$). They are utilised for the efficient and clean production of biomass- derived liquid
31 fuel 5-ethoxymethylfurfural (EMF) through direct etherification of hydroxymethylfurfural
32 (HMF) and one-pot conversion of fructose and other carbohydrates. High EMF yields of
33 93.1%, 62.2%, 23.9%, and 21.4% were obtained, when HMF, fructose, sorbose, and sucrose
34 were subjected as substrate, respectively. These catalysts were characterised by XRD, py-
35 FTIR, TGA, N_2 -physisorption, SEM and TEM-EDX mapping. Importantly, the catalyst could
36 be reused at least four times almost without a significant loss of activity.

37

38 Keywords

39 Biomass conversion; 5-hydroxymethylfurfural, 5-Ethoxymethylfurfural; Magnetic fibrous
40 silica core-shell; Heterogeneous catalysis

41

42

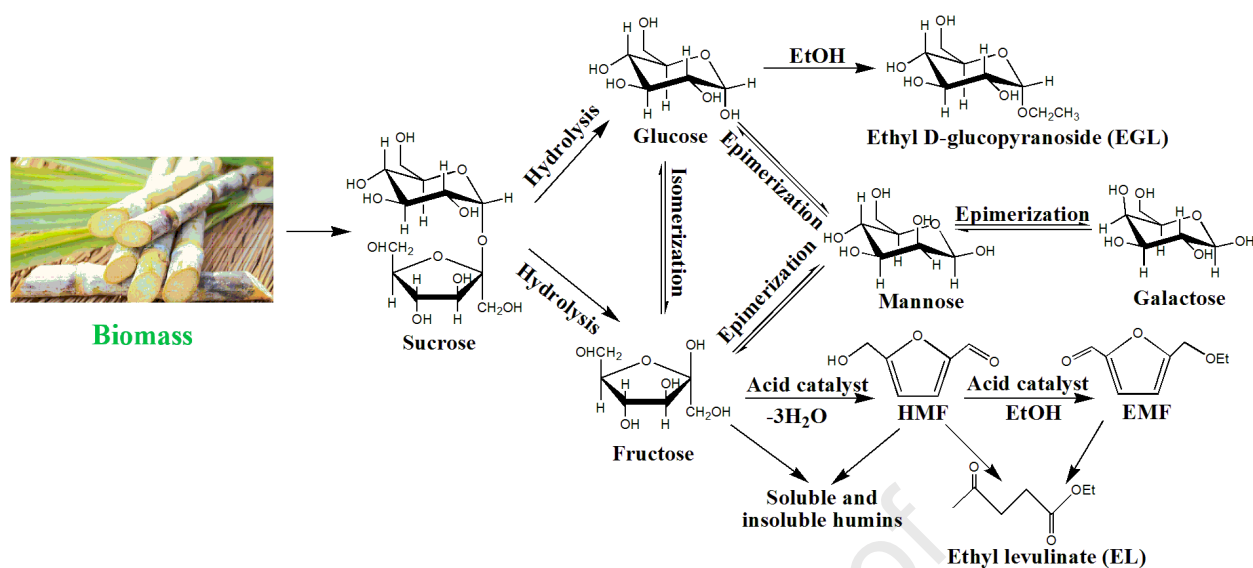
43

44

45

46 1. Introduction

47 For contemporary society, there are many concerns related to utilization of fossil resources
48 such as climate change, oil reserve depletion, rising demand for petroleum and consequently
49 rising prices. This has pushed many researchers towards the transformation of biomass
50 particularly carbohydrates into value-added and fine chemicals examples include 5-
51 hydroxymethylfurfural (HMF) which is considered as being in the top-10 versatile platform
52 chemicals by the US DOE (Department Of Energy) [[1], [2], [3], [4]]. Consequently, HMF
53 derivatives have a broad range of industrial applications. Take, furan-2,5-dicarboxylic acid
54 (FDCA) which can be used as monomer in the synthesis of polyesters in place of terephthalic
55 acid [5]. While, 2,5-diformylfuran (DFF), an oxidised product of HMF can be applied as
56 initiator to produce pharmaceuticals, fungicides and various polymers [[6], [7]]. Among all
57 biomass-derived furanic compounds, 5-ethoxymethylfurfural (EMF), an etherification product
58 of HMF, has possibly attracted the most attention as one of the most promising and green
59 renewable biofuels and fuel additives [[8], [9], [10]]. EMF with a higher octane number than
60 gasoline and diesel, has an energy density of 8.7 kWhL^{-1} , approximately equivalent to gasoline
61 (8.8 kWhL^{-1}) and diesel (9.7 kWhL^{-1}) but notably higher than ethanol (6.1 kWhL^{-1}). EMF can
62 also be utilized up to 25 wt% as a diesel-miscible biofuel (DMB). Moreover, it shows good
63 oxidation stability and low temperature fluidity [[11], [12], [13]]. The simplest pathway for the
64 synthesis of EMF is the direct etherification of HMF with ethanol through which a high yield
65 of EMF can be achievable quickly. For example, Yang et al. could achieve a EMF yield of 99%
66 with a full conversion of HMF within only 60 min [14]. However, one-pot synthesis of this
67 compound from carbohydrates, especially sugars as a cost-effective pathway (Scheme 1), is of
68 particular importance as dehydration of sugars to HMF, and etherification of HMF to EMF
69 reactions can be performed in the presence of acid catalysts [15].



70
71 Scheme 1. Proposed reaction pathways for the synthesis of EMF from HMF and various carbohydrates

72

73 Since heterogeneous catalysts have more advantages than homogeneous ones in the catalytic
74 biomass valorization and clean energy [[16], [17], [18]], various Brønsted and Lewis solid acid
75 catalysts have been designed and applied in the synthesis of EMF [19]. Recently, efforts have
76 been devoted to synthesis of EMF by employing heteropoly acid (HPAs) based catalysts
77 because of their strong Brønsted acidity, high proton conductivity, uniform acid sites and
78 thermal stability [[20], [21], [22]]. For example, a series of acid–base bifunctional hybrid
79 nanospheres were synthesized from the self-assembly of basic amino acids and
80 phosphotungstic acid and applied for the direct catalytic conversion of various carbohydrates
81 into EMF [23]. In another study, Liu et al. produced EMF from HMF and fructose using
82 mesoporous MCM-41 supported 12-tungstophosphoric acid (PTA) as the heterogeneous
83 catalyst [24].

84 In designing the solid acid catalysts factors such as an easily accessible high surface area which
85 boosts interaction between the active sites on the catalyst surface and reactive molecules and a
86 synergetic effect of Brønsted acid sites, like HPAs, which are supported over Lewis acid
87 carriers must be taken into account. On the other hand, it has been proved that the post-synthesis

88 grafting of Al species into a neutral Si framework of mesoporous silica, can improve the
89 stability and acidity of the catalyst [[25], [26]]. While it is known that aluminosilicate-based
90 catalysts has a remarkably synergistic effect with HPAs on the catalytic process. Atia et al.
91 showed that aluminosilicate-supported HPAs was more active than silica-supported catalysts
92 and bulk HPAs in glycerol dehydration [27]. Nandhini and coworkers illustrate that, the
93 presence of aluminum in MCM-41 mesoporous silica can impose better hydrophilic property
94 to entrap more HPA units thereby increasing the acidity of the resultant solid acid catalyst [28].
95 Besides, in more recent years, magnetic nanoparticles (MNPs) have also attracted extensive
96 attention for their promising applications, particularly in heterogeneous catalysis of organic
97 reactions because they are inexpensive with low toxicity and can easily be separated and
98 isolated from the reaction mixture by applying an external magnet allowing reuse of the catalyst
99 [[29], [30], [31]]. This feature makes the catalyst suitable for industrial applications [[32],
100 [33]]. For instance, Zhang et al. by using magnetically recoverable $\text{Fe}_3\text{O}_4@\text{SiO}_2\text{-SO}_3\text{H}$
101 demonstrated that EMF could achieve from fructose and inulin [34]. In another work, they
102 studied the production of EMF through direct etherification of HMF and one-pot conversion
103 of fructose by $\text{Fe}_3\text{O}_4@\text{SiO}_2$ nanoparticles supported HPA as catalyst [35]. Yuan et al. explored
104 the conversion of carbohydrates into EMF over $\text{Fe}_3\text{O}_4@\text{C-SO}_3\text{H}$ [36]. But an important point
105 to mention about these magnetic catalysts is the lack of high surface area and since high
106 surface-to-volume ratio of a heterogenous catalyst is one of the primary factors in catalysis, the
107 efficiency of above mentioned magnetic catalysts is limited. In 2010, Polshettiwar et al.
108 reported synthesis of fibrous nano-silica (KCC-1) [37]. KCC-1 has a high surface area, large
109 open pore structure, and high thermal and hydrothermal stabilities. The synthesis of magnetic
110 core-shell fibrous silica nanocomposite $\text{Fe}_3\text{O}_4@\text{SiO}_2@\text{KCC-1}$, which has both the unique
111 properties of KCC-1 and the physical properties of magnetic materials, reported by Yu et al
112 [38]. Hence, $\text{Fe}_3\text{O}_4@\text{SiO}_2@\text{KCC-1}$ due to its exclusive physical properties such as easily

113 accessible high surface area and subsequent ease of further functionalization, excellent solvent
114 dispersibility, and retrievability allows it to be highly efficient as a supported catalysts [[39],
115 [40]].

116 Considering all above, herein we design, synthesise and characterise a novel, green, and
117 magnetically recyclable heterogeneous acid catalyst, $\text{Fe}_3\text{O}_4@\text{SiO}_2@\text{KCC-1}/\text{Al}/\text{PTA}$ with high
118 surface area, consisting of PTA with a Keggin structure as an efficient source of Brønsted acid
119 [20] and aluminium as Lewis acid and mesoporous silica stability enhancer. Here, the first
120 report on the use of this type of magnetic catalyst in the biomass valorisation reactions has been
121 reported [29]. The performance of the catalyst is evaluated in direct HMF etherification and
122 one-pot conversion of carbohydrates for the synthesis of EMF.

123 **2. Experimental**

124 2.1. Chemicals and reagents

125 In this study tetraethylorthosilicate (TEOS, 98%), sodium acetate anhydrous (NaOAc), sodium
126 citrate tribasic dihydrate (NaCit), aqueous ammonia ($\text{NH}_3\cdot\text{H}_2\text{O}$, 28%), urea, ethylene glycol,
127 aluminium nitrate nonahydrate ($\text{Al}(\text{NO}_3)_3\cdot 9\text{H}_2\text{O}$), phosphotungstic acid, 5-
128 hydroxymethylfurfural ($\geq 99\%$), 5-ethoxymethylfurfural (97%), cyclohexane, 1-pentanol,
129 ethanol, fructose, glucose, mannose, sucrose, galactose and sorbose were each obtained from
130 Sigma-Aldrich Ireland. Hexadecyltrimethylammonium bromide (CTAB) was obtained from
131 VWR International Ltd. $\text{FeCl}_3\cdot 6\text{H}_2\text{O}$ was purchased from Fisher Scientific UK.

132 2.2. Synthesis of Fe_3O_4 (F) magnetic nanoparticles (MNPs)

133 Fe_3O_4 MNPs with a mean diameter of approximately 100 nm were synthesized based on a
134 previously published procedure [41]. Briefly, 3.25 g of $\text{FeCl}_3\cdot 6\text{H}_2\text{O}$ and 1.2 g NaCit were first
135 dissolved in 80 mL of ethylene glycol under vigorous magnetic stirring for 1 h to form a clear
136 solution. Then 6 g of NaOAc was added to this solution and vigorously stirred for another 1 h.

137 The final mixture was heated in a Teflon-lined stainless-steel autoclave for 10 h at 200 °C.
138 Afterwards the autoclave was allowed to be naturally cooled to room temperature. The black
139 Fe₃O₄ MNPs were collected by a magnet, followed by several rinsing with deionized water and
140 ethanol and oven-dried at 60 °C overnight.

141 2.3. Synthesis of Fe₃O₄@SiO₂ (FS) core-shell nanospheres

142 The SiO₂ layer was coated on Fe₃O₄ MNPs through a modified Stöber method. In a typical
143 synthesis core-shell structured Fe₃O₄@SiO₂ nanospheres, one gram of as-synthesized Fe₃O₄
144 particles were added to a three-neck round-bottom flask and homogeneously dispersed in a
145 mixture solution of 400 mL ethanol, 100 mL deionized water and 6 mL of concentrated
146 ammonia by ultra-sonication for 1 h. Afterward, 3 mL of TEOS was dropwise added to the
147 mixture under continuous mechanical stirring and the reaction was allowed to proceed for 6 h
148 at room temperature. The produced Fe₃O₄@SiO₂ core-shell product was magnetically collected
149 and washed with ethanol and deionized water, and vacuumed dried at 60 °C overnight.

150 2.4. Synthesis of Fe₃O₄@SiO₂@KCC-1 (FSK) core-shell microspheres

151 For FSK core-shell dendritic fibrous silica microspheres, briefly, 250 mg of FS nanospheres
152 was dispersed into a mixture solution A, containing 30 mL DI and 0.3 g of urea under ultra-
153 sonication for 30 min. Solution B was formed by adding 0.5 g of CTAB into 30 mL of
154 cyclohexane and 0.75 mL of *n*-pentanol. Then, solutions A and B were mixed under mechanical
155 stirring at room temperature. 1.25 g TEOS was added to the upper solution dropwise and after
156 1 h of stirring, the resulting mixture was transferred to a 100 mL Teflon-lined autoclave and
157 heated for 5 h at 120 °C. The solid product was then collected using a magnet, washed with
158 ethanol, dried at 60 °C and subsequently calcined at 550 °C for 6 h to remove organic moieties.

159 2.5. Preparation of Fe₃O₄@SiO₂@KCC-1/Al/PTA_x (FSK/Al/PTA_x) catalysts

160 Different (10, 20, 30 and 40%) weight percentages of PTA with a ratio of 10% (w/w) of
161 aluminium supported onto dendritic silica shell of FSK (denoted as FSK/ Al₁₀/PTA_x, where x
162 represents the weight percentages of the PTA) were prepared in two steps by a wetness
163 impregnation method. Firstly, one gram of FSK was dispersed in an aqueous solution of
164 aluminium nitrate with a predetermined Al-FSK (10 % w/w) by sonication for 1 h. The mixture
165 was then dried using a vacuum oven overnight. Finally, the resultant material was calcined at
166 500 °C for 5 h in air to obtain FSK/Al. In a second step, to allow the preparation of a series of
167 catalysts with different PTA loadings varying from 10 to 40 wt%, as synthesized FSK/Al was
168 dispersed in 5 mL of ethanol containing a calculated amount of PTA with the assistance of
169 ultrasonic for 1 h. Samples were heated at 60 °C in a vacuum oven to remove methanol and
170 further dried at 100 °C for 8 h, followed by calcination at 300 °C for 2 h. The loading amount
171 of PTA was calculated according to the equation (1):

$$\text{Loading amount (\%)} = [\text{Weight of PTA} / \text{Weight of PTA} + \text{Weight of FSK/Al}] \times 100\% \quad (1)$$

172

173 2.6. Characterization methods

174 Powder X-ray diffraction patterns of the samples with Cu K α radiation ($\lambda = 0.154$ nm, 40 kV,
175 40 mA) were recorded on a PANalytical Empyrean diffractometer. All XRD patterns were
176 collected in the 2θ range of 10-90°. The acidity measurements of the catalysts after pyridine
177 adsorption were carried out on a Nicolet Nexus Fourier transform infrared (FTIR) spectrometer
178 equipped with an attenuated total reflectance accessory (ATR). The measurements were
179 recorded in the wavenumber range 1400–1700 cm⁻¹. Thermogravimetric analysis (TGA) was
180 performed using a TGA-4000 Thermogravimetric Analyser (Perkin-Elmer Instruments,
181 Beaconsfield, Bucks, UK). The samples were heated from room temperature to 800 °C at a
182 heating rate of 10 °C.min⁻¹ under a nitrogen atmosphere. Field-emission electron microscope
183 (FE-SEM, Hitachi SU8030, Japan), high-resolution transmission electron microscopy

184 (HRTEM) and energy-dispersive X-ray (EDX) mapping (JEOL JEM-2011 F electron
185 microscope) were employed to observe the surface topography, morphology, structure and
186 composition of the magnetic samples. The textural properties of the core-shell nanoparticles
187 were evaluated by N₂ adsorption/desorption technique using a Quantachrome Autosorb-1
188 Instrument. Before the analysis, the samples were vacuum degassed at 250 °C for 5 h. While
189 specific surface area and pore size distribution were calculated based on the Brunauer–
190 Emmett–Teller (BET) and Barret–Joyner–Halende (BJH) methods, respectively.

191 2.7. Catalytic etherification reaction procedure

192 In a typical etherification reaction, one mmol of HMF (or carbohydrate), FSK/Al/PTA (40 mg)
193 and ethanol (5 mL) were transferred to an ACE pressure tube (Sigma-Aldrich, 15 mL, 10.2 cm
194 long). The tube was immersed in a preheated oil bath, and the reaction mixture was vigorously
195 stirred at 600 rpm for a given time and at a given temperature. Subsequently, the reactor tube
196 was quickly quenched in an ice-water bath. The catalyst was then magnetically collected from
197 the reaction mixture and the product phase was analysed by high-performance liquid
198 chromatography (HPLC, Agilent 1260 series) using a C18 reverse-phase column (200 mm ×
199 4.6 mm, 5 μm). A 0.1 wt% acetic acid aqueous solution and acetonitrile (V: V = 85:15) mobile
200 phase was employed as the mobile phase at 30 °C with a flow rate of 0.5 mL.min⁻¹. The
201 samples were quantified using an external standard calibration curve method.

202 The product yield, conversion of substrate and product selectivity were calculated as following
203 equations:

$$\text{Yield (\%)} = [\text{moles of EMF produced} / \text{initial moles of substrate}] \times 100\% \quad (2)$$

$$\text{Conversion (\%)} = [1 - (\text{final moles of substrate} / \text{initial moles of substrate})] \times 100\% \quad (3)$$

$$\text{Selectivity (\%)} = [\text{yield} / \text{conversion}] \times 100\% \quad (4)$$

204

205 **3. Results and discussion**

206 3.1. Catalyst characterization

207 3.1.1. Nitrogen adsorption/desorption analysis

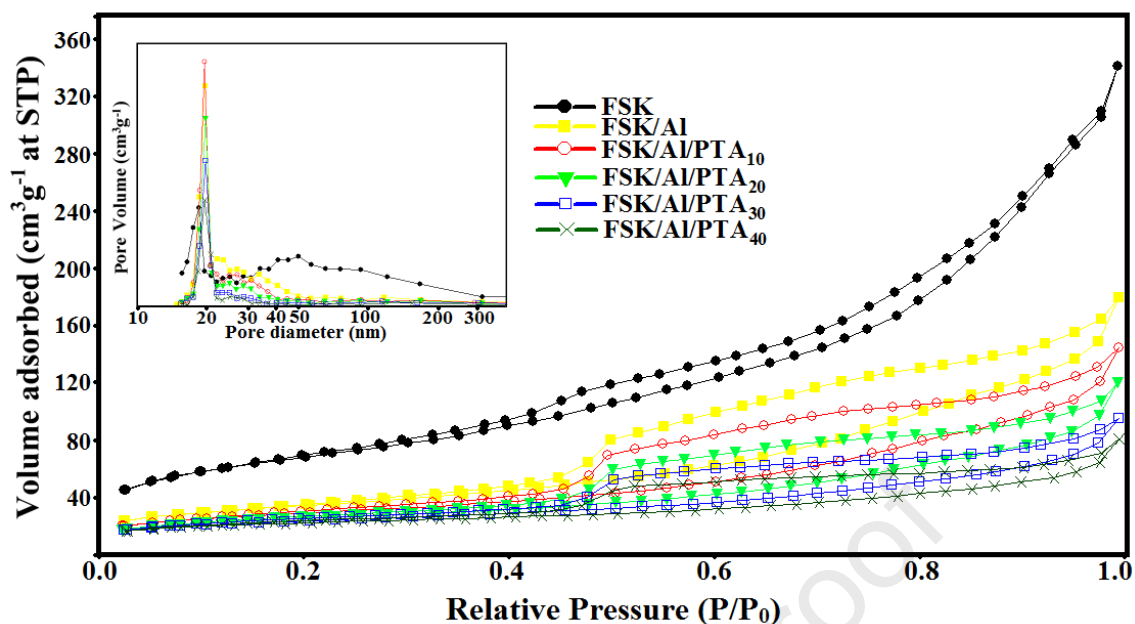
208 Fig. 1 displays the N₂ sorption isotherms and pore size distribution of all core-shell
 209 microspheres. All samples exhibited type IV isotherms which is compatible with the literature
 210 on standard fibrous silica spheres. In addition, an obvious hysteresis loop of type H₁ in the P/P₀
 211 range of 0.4–1.0 can be seen, indicating solid evidence of mesoporous cylindrical or rod-like
 212 pores. It is inferred from the curves that the mesoporous texture of the microspheres is protected
 213 during surface modification and this further evidenced by TEM images (Fig. 2). BET surface
 214 area, total pore volume, and BJH pore diameter are summarized in Table 1. FSK has the highest
 215 surface area and pore volume but a gradual reduction occurs as the content of PTA increases.
 216 This is explained by the diffusion of PTA molecules in the dendritic pores of the microspheres
 217 during the impregnation process, resulting in pore blockage/coverage. These reductions in
 218 surface area and pore volume for the FSK/Al can be due to the incorporation of aluminium
 219 atoms in the fibrous silica shell. It is also worth noting that the pore diameter of FSK decreases
 220 after impregnation with aluminium. It is postulated that this arises due to differences in ionic
 221 radii of the Si⁴⁺ and Al³⁺, and that the substitution of Si-O- by Al-O- leads to changes in the
 222 bond angles in the mesoporous shell which ultimately effects on diameter of the pores. This
 223 complements findings in other studies [[42], [43]].

224 Table 1. Textural parameters of core-shell materials

Sample	Surface area (m ² /g)	Pore volume (cm ³ /g)	Pore diameter (nm)
FSK	242	0.49	18.5
FSK/Al	194	0.30	19.7
FSK/Al/PTA ₁₀	159	0.24	19.6
FSK/Al/PTA ₂₀	127	0.19	19.7
FSK/Al/PTA ₃₀	99	0.14	19.7
FSK/Al/PTA ₄₀	77	0.11	19.5

225

226

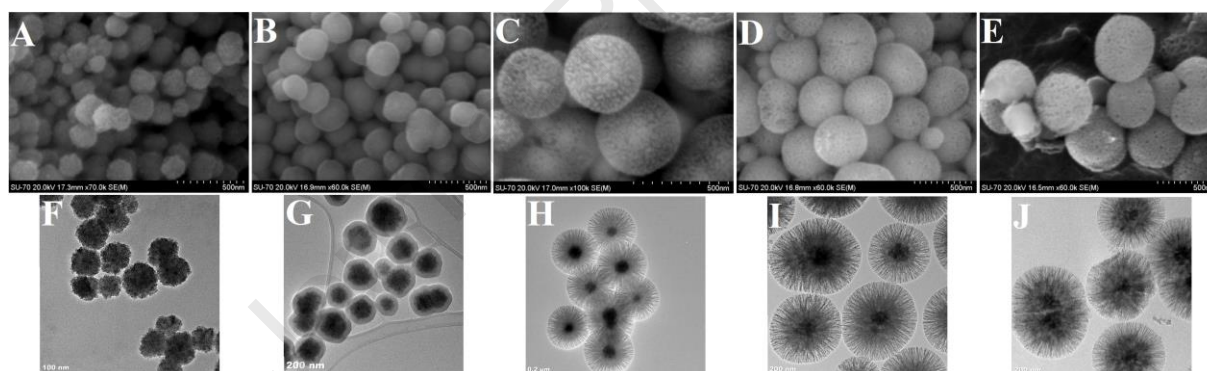


227
228 Fig. 1. N₂ adsorption-desorption isotherms and BJH pore-size distribution curves (inset) of core-shell
229 structures

230
231 3.1.2. SEM, TEM and elemental mapping analysis

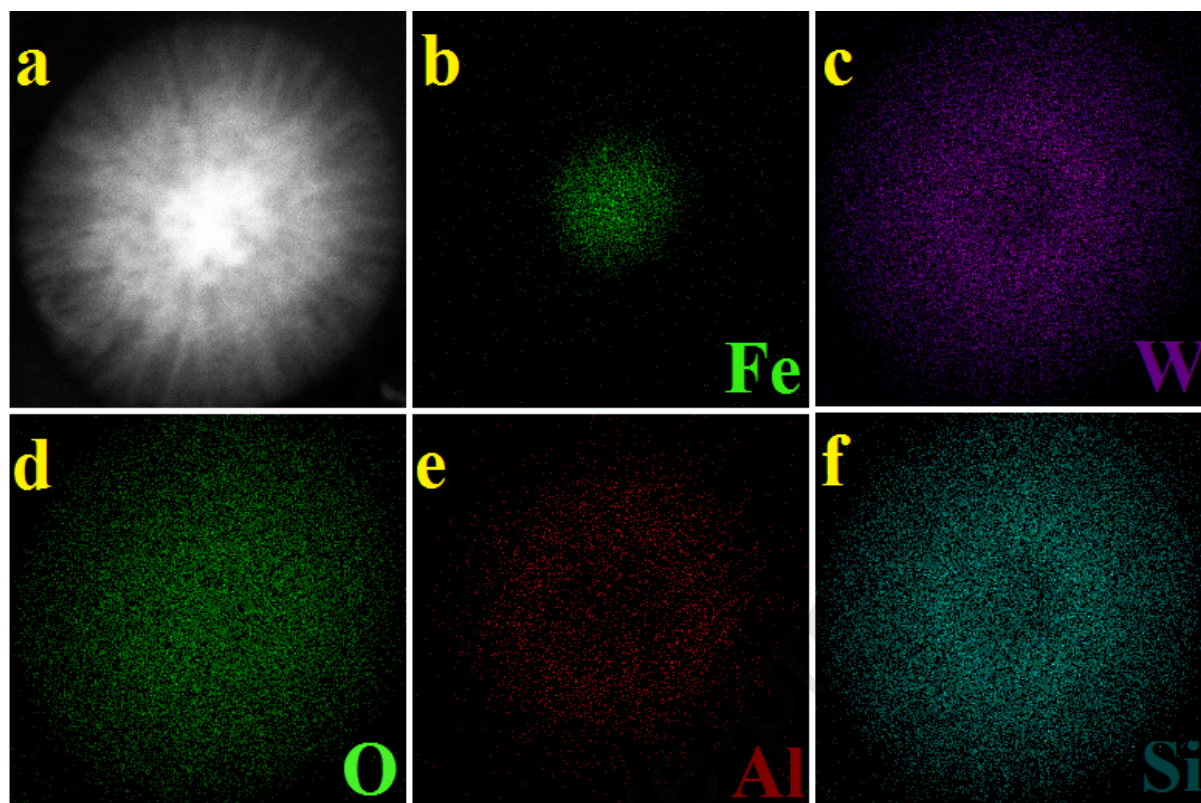
232 The morphology, size, shape and structural features of as-synthesized precursor Fe₃O₄ MNPs
233 to final Fe₃O₄@SiO₂@KCC-1/Al/PTA core-shell microspheres were evaluated by SEM and
234 TEM analysis (Fig. 2). The Fe₃O₄ MNPs with a mean diameter of 100 nm exhibit a spherical
235 morphology and uniform size distribution with slightly rough surfaces morphologies (Fig. 2 A
236 and F). Fig. 2 (B and G) show that after coating a SiO₂ shell in order to prevent the
237 agglomeration and improve the dispersion, a gray layer is fabricated on the pristine magnetic
238 nanoparticles, making the surface of core-shell NPs smooth. It is obvious that highly uniform
239 and monodisperse nanoparticles are obtained, and each FS core shell sphere contains only one
240 Fe₃O₄ core at the center with a shell thickness of about 25 nm. In the next step, the FS core-
241 shell NPs were applied as core part and KCC-1 as a dendritic mesoporous silica shell, was
242 successfully expanded on it, growing from the center to outside in all directions (Fig. 2 C and
243 H). The morphology was uniform microspheres with a wrinkled radial structure. The average
244 diameter of the FSK core shell was determined to be about 400 nm. As shown in Fig. 2 (D, E,
245 I and J), although after two steps of functionalization for obtaining FSK/Al/PTA catalyst, the

246 core shell structure remained intact and still exhibited uniform shape and good monodispersity,
247 however roughness of microspheres increased, attributing to differences in ionic radii of the
248 Si^{4+} and Al^{3+} in the framework and also encapsulation of Keggin-type structure of PTA in
249 dendritic fibrous shell which can be observed in SEM images (Fig. 2 G and I). In addition,
250 EDX mapping analysis was applied to a single microsphere to confirm the presence of elements
251 and their distribution within the FSK/Al/PTA catalyst. STEM (scanning transmission electron
252 microscopy) images (Fig.3 a) and distribution mapping (Fig.3 b-f) show that an Fe enriched
253 area (b) is clearly concentrated in the core area, and it is surrounded by Si (Fig.3 f), which is
254 more condense in the center, representing the thin silica layer on the Fe_3O_4 core. The O element
255 (Fig.3 d) is observed in all regions. While Al (Fig.3 e) and W (Fig.3 c) atoms are also well
256 dispersed throughout the dendritic mesoporous silica shell.



257

258 Fig. 2. SEM (A-E) and TEM (F-J) images of Fe_3O_4 (A and F), $\text{Fe}_3\text{O}_4@SiO_2$ (B and G),
259 $\text{Fe}_3\text{O}_4@SiO_2@KCC-1$ (C and H), $\text{Fe}_3\text{O}_4@SiO_2@KCC-1/Al$ (D, I) and $\text{Fe}_3\text{O}_4@SiO_2@KCC-1/Al/PTA$
260 (E and J)



261

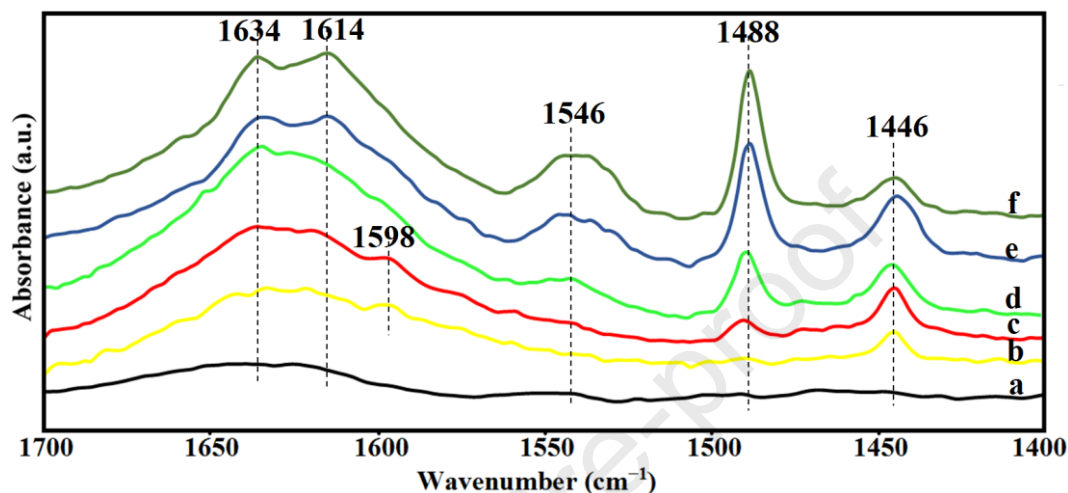
262 Fig. 3. STEM image of the FSK/Al/PTA microdisphere (a) and Fe, Si, O, Al and W elemental-mapping
 263 images.

264

265 3.1.3. Py-FTIR analysis

266 FTIR studies of adsorbed pyridine (Py-FTIR) spectra of samples were recorded to distinguish
 267 and evaluate type of acidic sites. As shown in Fig. 4 a, no adsorption peaks were observed for
 268 FSK, only a weak broad peak at $1600-1670\text{ cm}^{-1}$ that can be attributed to adsorbed water
 269 molecules and pyridine adsorbed on silanol (Si-OH) groups on the surface of the sample which
 270 have relatively weak acidity, through hydrogen bonding (Py-H^+) [[44], [45]]. Two additional
 271 peaks in FSK/Al (Fig.4 b) located at 1598 and 1446 cm^{-1} are ascribed to the interaction of
 272 pyridine to Lewis acid sites [45]. In Fig. 4 (e and f) for the samples impregnated by higher
 273 loadings of PTA (FSK/Al/PTA₃₀ and FSK/Al/PTA₄₀), the bands appeared at 1634 , 1614 and
 274 1546 cm^{-1} are associated with the contribution of pyridinium (Py-H^+) ions, representing the
 275 Brønsted acid sites. whereas the band at 1488 cm^{-1} is corresponded to both Lewis and Brønsted
 276 acid sites. However, for FSK/Al there is no band at 1488 cm^{-1} , corresponding to a Lewis acid

277 site. While for FSK/Al/PTA₁₀ (Fig. 4 c) and FSK/Al/PTA₂₀ (Fig. 4d) there are no pyridinium
 278 ion vibrations at 1634 cm⁻¹ and therefore, one can conclude that the band at 1488 cm⁻¹ is mostly
 279 attributed to the interaction of pyridine to Brønsted acid site. It is worth noting that the intensity
 280 of all the bands enhanced as the concentration of PTA increased.



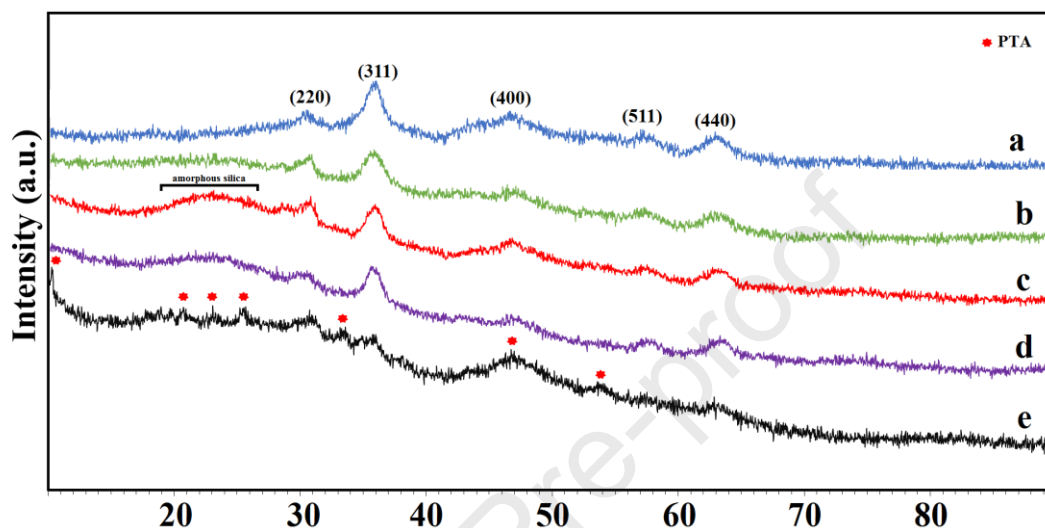
281
 282 Fig. 4. Pyridine-FTIR spectra of a) FSK, b) FSK/Al, c) FSK/Al/PTA₁₀, d) FSK/Al/PTA₂₀, e)
 283 FSK/Al/PTA₃₀ and f) FSK/Al/PTA₄₀ microspheres

284

285 3.1.4. XRD analysis

286 The composition and crystallinity of the as synthesized magnetic samples consisting of Fe₃O₄,
 287 FS, FSK, FSK/Al and FSK/Al/PTA were investigated by XRD analysis. The wide-angle XRD
 288 pattern of the samples are shown in Fig. 5. As can be seen, for all samples there are five main
 289 diffraction peaks at $2\theta = 31^\circ, 36^\circ, 47.1^\circ, 57.5^\circ$ and 63.2° , which can be assigned to (220), (311),
 290 (400), (511) and (440) crystal planes of standard Fe₃O₄ (JCPDS No. 19-0629), respectively,
 291 indicating that the Fe₃O₄ MNPs were well maintained in the silica matrix. In addition to the
 292 Fe₃O₄ peaks, the XRD pattern of other samples presented a broad XRD peak at low diffraction
 293 angles ($2\theta = 16-27^\circ$), which is attributed to the amorphous silica. However, such a broad
 294 diffraction peak was not observed in the XRD patterns of FS sample likely because of the low
 295 content of silica which was also reported in other studies. The XRD pattern of FSK/Al/PTA
 296 catalyst shows additional diffraction peaks at $2\theta = 10.35^\circ, 20.67^\circ, 23.06^\circ, 25.66^\circ, 33.59^\circ$,

297 46.98° and 54.23° corresponding to the cubic Keggin-type structure of PTA. Meanwhile it
 298 should be noted that in the FSK/Al/PTA catalyst the intensity of peaks corresponding to iron
 299 oxide decrease due to the impregnation procedure and deposition of PTA on the surface of the
 300 catalyst.



301 Fig. 5. Wide-angle XRD patterns of a) Fe_3O_4 , b) FS, c) FSK, d) FSK/Al and e) FSK/Al/PTA samples
 302

303

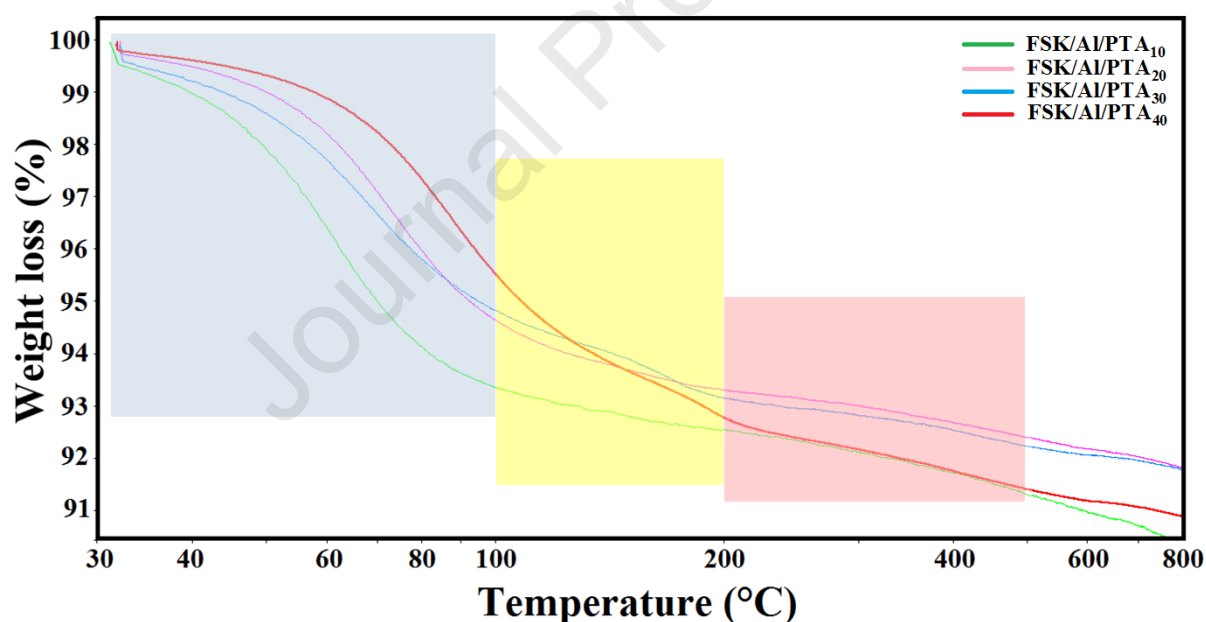
304 3.1.5. Thermogravimetric analysis

305 A potentially important advantage of supporting PTA on mesoporous silica materials is
 306 enhancing thermal stability for the PTA salts. Hence, thermogravimetric analysis of the series
 307 of FSK/Al₁₀/PTA_x catalysts prepared in this work was performed to investigate mass loss and
 308 thermal stability. The TGA results are displayed in Fig. 6. According to these curves, there
 309 were three key mass loss stages for all the samples. The first weight loss was related to the loss
 310 of adsorbed water molecules. This water release ranged from 30 °C up to 100 °C (highlighted
 311 blue) which for FSK/Al₁₀/PTA₁₀ was the maximum (6.7%) and it was the lowest for the
 312 FSK/Al₁₀/PTA₄₀ (4.5%). A second weight loss in the temperature range of 100 °C to near 200
 313 °C (highlighted yellow) was ascribed to the loss of hydrogen bonded water molecules and the
 314 water of crystallization from between individual Keggin cluster ions [46], which are
 315 hydrothermally stable up to 350 °C. The catalyst with 40% of PTA had the maximum weight

316 loss in the second range (about 3.3%). The third stage occurred over a range of temperatures
 317 between 200 and 500 °C (highlighted pink) and is a low and gradual weight loss for all
 318 catalysts. This could have several reasons: (i) high stability of Keggin anions of PTA; (ii) the
 319 water molecules that were in the mesopores could not escape due to the maximum presence of
 320 Keggin anions in the mesopore channels [47]; (iii) decomposition of pure PTA into simple
 321 oxides could occur at 485 °C. Therefore, it can be concluded that decomposition of Keggin
 322 anions in this temperature range was not remarkable [48]; (iv) decomposition of PTA at higher
 323 temperatures leading to the formation of tungsten trioxide which is thermally stable [47]:



324



325 Fig. 6. Thermal gravimetric analysis of FSK/Al/PTA₁₀, FSK/Al/PTA₂₀, FSK/Al/PTA₃₀ and
 326
 327 FSK/Al/PTA₄₀

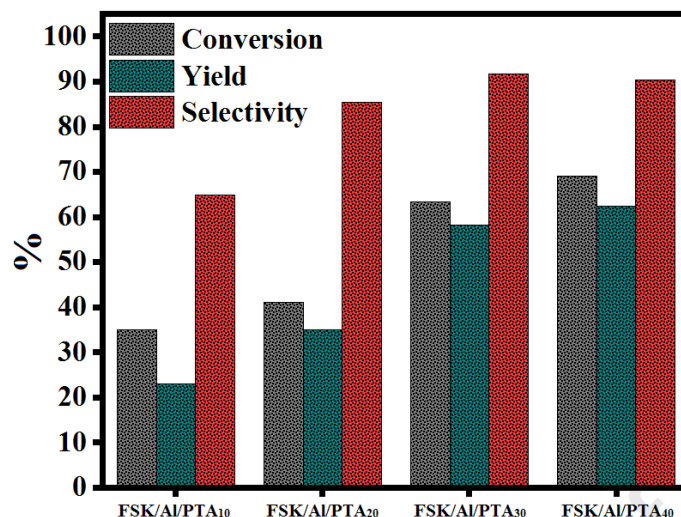
328

329 3.2. Catalytic activity in etherification of HMF into EMF

330 3.2.1. Effect of PTA content in the catalyst

331 To evaluate the effect of % loading of PTA, an etherification reaction was carried out using
 332 FSK/Al/PTA₁₀, FSK/Al/PTA₂₀, FSK/Al/PTA₃₀ and FSK/Al/PTA₄₀ catalysts. The results are

333 shown in Fig. 7. The reaction was conducted over 40 mg of catalyst and other operating
334 parameters including temperature and time were kept constant at 100 °C and 1 h, respectively.
335 From the figure, the percentage of yield and conversion rises gradually as the % loading of
336 PTA increases which can be attributed to the increment amount of acid sites. The catalyst with
337 10 wt% PTA was able to convert 35.7% of HMF with 23.2% of EMF yield and 35% of the
338 yield was obtained by FSK/Al/PTA₂₀, while FSK/Al/PTA₃₀ catalyst converted 63.4% of HMF
339 with 58.2% of EMF yield. Although the maximum conversion (69.1%) and yield (62.5%) was
340 achieved for the catalyst with 40% PTA due to proportional enhancement in the amount of acid
341 sites, but they were not noticeable compared to those of FSK/Al/PTA₃₀ and also a lower
342 selectivity was seen for FSK/Al/PTA₄₀. The morphology and subsequently, the surface area
343 and total acidity of the catalysts could be behind this difference in catalytic activity. Albeit
344 based on the TEM and SEM images (Fig. 2) the structure of microspheres overall remained
345 intact. BET results (Table 1) reveal that surface area reduced as the content of PTA increased.
346 Subsequently the amount of active acid sites in the catalyst that are accessible declined, leading
347 to an insignificant increase in the yield of EMF. Therefore, all further experiments were
348 conducted using the catalyst containing 30% loading of PTA as this was found to be the most
349 efficient catalyst.

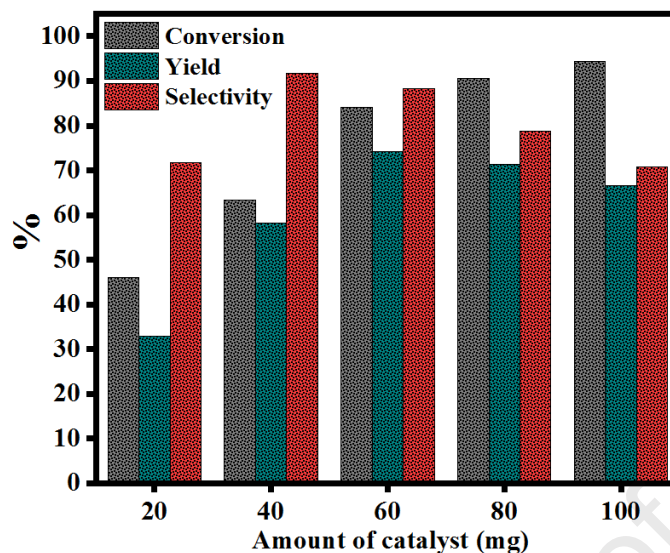


350 Fig. 7. Effect of PTA content on the HMF etherification. Reaction conditions: (HMF: 1 mmol, ethanol:
 351 5 mL, catalyst amount: 40 mg, temperature: 100 °C, reaction time: 1 h).
 352
 353

354 3.2.2. Effect of catalyst amount

355 Fig. 8 shows the effect of FSK/Al/PTA₃₀ catalyst amount ranging from 20 to 100 mg on the
 356 EMF production from HMF whilst the reaction time and temperature were fixed at 1 h and 100
 357 °C. An increase in the conversion (46-94.3%) was achieved by increasing the catalyst dose
 358 from 20 to 100 mg, and this was attributed to the availability of a higher number of catalytically
 359 active sites. Only 33% of EMF yield was obtained using 20 mg catalyst whereas a maximum
 360 of 74.2% of the yield was achieved utilizing 60 mg. When the catalyst loading was higher than
 361 60 mg a drop in EMF yield and selectivity occurred with, for example 100 mg achieving 66.7%
 362 and 70.7%, respectively. This reduction is caused by the excessive amount of active sites and
 363 is mostly related to the formation of byproducts such as ethyl levulinate (EL) or undesired
 364 humins (scheme 1). Therefore, 60 mg was chosen as the optimum amount of the catalyst to
 365 produce EMF.

366

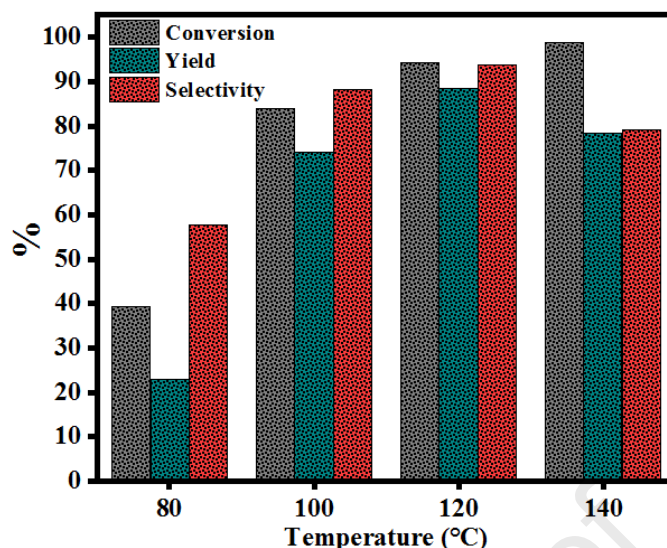


367 Fig. 8. Effect of catalyst amount on the HMF etherification. Reaction conditions: (HMF: 1 mmol,
 368 ethanol: 5 mL, temperature: 100 °C, reaction time: 1 h).
 369

370

371 3.2.3. Effect of reaction temperature

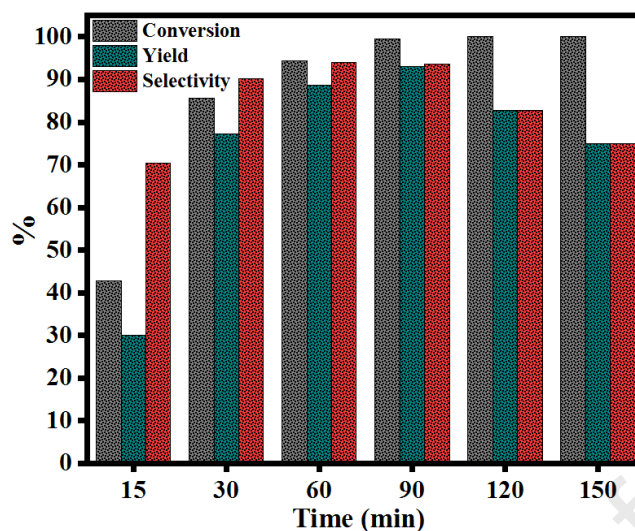
372 Since temperature seems to have a significant impact on the etherification reaction, the catalytic
 373 performance of FSK/Al/PTA₃₀ under varying temperatures (80-140 °C) was assessed after 1 h
 374 reaction time to study the effect of reaction temperature. As evidenced by Fig. 9, HMF
 375 conversion and yield of EMF are considerably affected by the reaction temperature. At 80 °C,
 376 the selectivity for EMF was 22.7% with 39.3% conversion of HMF. The percentages of HMF
 377 conversion and corresponding yield of EMF were improved with the increase of reaction
 378 temperature up to 120 °C, to a maximum of 94.3 and 88.6%, respectively, and afterwards, when
 379 the temperature was raised to 140 °C the conversion of HMF increased to 99%, meanwhile the
 380 EMF yield decreased from 88.6 to 78.5%. Likewise, the selectivity of EMF at 140 °C was lower
 381 than those attained at 100 and 120 °C. The reasons for the reduction of EMF yield and
 382 selectivity can be ascribed to the hydrolytic degradation of HMF and EMF in acidic conditions
 383 [49]



384 Fig. 9. Effect of reaction temperature on the HMF etherification. Reaction conditions: (HMF: 1 mmol,
 385 ethanol: 5 mL, catalyst amount: 60 mg, reaction time: 1 h).
 386
 387

388 3.2.4. Effect of reaction time

389 Fig. 10 illustrates the results of the effect of time on the catalytic etherification reaction. Similar
 390 to reaction temperature, EMF yield increased quickly from 42.8% to 77.3% with increasing
 391 reaction time from 15 to 30 min in the presence of 60 mg of FSK/Al/PTA₃₀ catalyst at 120 °C.
 392 Both HMF conversion and EMF yield were enhanced with the prolonging of reaction time up
 393 to 90 min and reached 99.5% and 93.1%, respectively. Although the conversion of HMF was
 394 completed at the longer reaction time, a drop in EMF yield (82.8% to 74.9% in 120 and 150
 395 min, respectively) was found due to the subsequent reaction to produce EL and also the
 396 production of both soluble and insoluble humins which also formed at higher reaction
 397 temperatures.

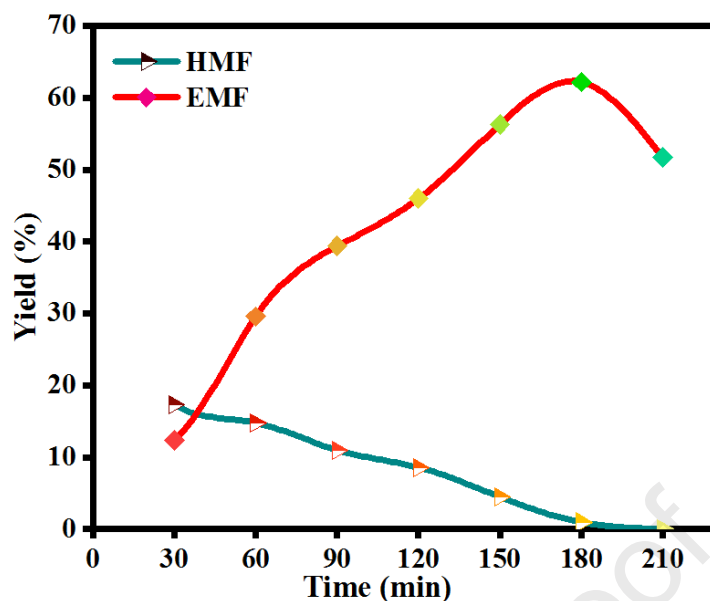


398 Fig. 10. Effect of reaction time on the HMF etherification. Reaction conditions: (HMF: 1 mmol,
 399 ethanol: 5 mL, catalyst amount: 60 mg, reaction temperature: 120 °C).
 400

401

402 3.3. One-pot production of EMF from fructose

403 A high yield of EMF was successfully acquired from etherification of HMF, however the
 404 production of EMF from fructose through one-pot synthesis is more attractive due to the
 405 combination of acid-catalyzed dehydration-etherification reactions which save energy and
 406 time. Therefore, one-pot synthesis of EMF from fructose was investigated under the optimal
 407 conditions found for the etherification of HMF (i.e. 60 mg of catalyst, and 120 °C) and the
 408 reaction results as functions of the reaction time are displayed in Fig. 11. Contrary to the results
 409 of direct etherification of HMF, EMF yield produced from fructose was much lower so that
 410 after 30 min 12.4% of EMF yield and 17% of HMF yield were obtained. However, when the
 411 reaction time was prolonged to 180 min almost all the HMF converted while the EMF gradually
 412 increased, reaching a maximum value of 62.2%. Longer reaction times led to a decrease of the
 413 EMF yield (51.7%), owing to transformation of EMF [50].



414 Fig. 11. Effect of reaction time on the EMF production from fructose. Reaction conditions: (fructose:
 415 1 mmol, ethanol: 5 mL, catalyst amount: 60 mg, reaction temperature: 120 °C).
 416

417

418 3.4. One-pot production of HMF and EMF from various carbohydrates

419 In order to gain a deeper insight into the applicability of the catalyst and substrate of our
 420 catalytic system, one-pot production of EMF from various low-cost carbohydrates (including
 421 glucose, mannose, galactose, sorbose and sucrose) were investigated under the optimized
 422 conditions achieved for fructose (i.e. 60 mg of catalyst, 120 °C, 3 h, 1 mmol substrate and 5
 423 mL ethanol). The results are listed in Table 2. Although a high yield of EMF (62.2%) was
 424 produced from fructose but when glucose as an aldose sugar was subjected as substrate, a trace
 425 amounts of HMF and no peak for EMF were detected by HPLC. The reason of this is uphill
 426 isomerization of glucose to fructose under acidic conditions which is a primary stage for the
 427 synthesis of EMF in ethanol [51]. It has been reported that ethyl D-glucopyranoside (EGL) is
 428 the major product of ethanolysis of glucose under an acidic condition through the facile and
 429 quick promotion of glycosylation of the -OH group at C₁ in glucose (scheme 1) [52]. Likewise,
 430 for other aldose-based carbohydrates (mannose and galactose) the acid catalyst was almost
 431 inert for the synthesis of EMF and only trace amounts of HMF and EMF were detected. In
 432 addition, since one molecule of sucrose contains one glucose and one fructose unit in its

433 structure, when sucrose as the most abundant and cheapest disaccharide was employed as
 434 feedstock, the yield of HMF and EMF were 6% and 21.4%, respectively. Nevertheless, the
 435 catalyst could effectively catalyze the hydrolysis of sucrose. Interestingly, by using sorbose as
 436 the starting material, HMF and EMF yields were 8.5% and 23.9%, respectively. These results
 437 confirm that our catalytic system is highly efficient for the transformation of ketose
 438 carbohydrates such as fructose and sorbose into EMF, but is unsuitable for aldose sugars.

439 Table 2. synthesis of EMF from various carbohydrates

Entry	Substate	EMF yield (%)	HMF yield (%)
1	Fructose	62.2	1
2	Glucose	ND*	trace
3	Sucrose	21.4	6
4	Mannose	trace	trace
5	Galactose	trace	trace
6	Sorbose	23.9	8.5

440 Reaction conditions: (substrate: 1 mmol, ethanol: 5 mL, catalyst amount: 60 mg, reaction temperature:
 441 120 °C, time: 3 h), *ND: not detected.

442
 443

444 3.5. Catalyst reusability

445

446 Reusability and recycle stability of the catalyst are key features to evaluate the efficiency of
 447 catalyst for its industrial application in practical biomass transformation. Hence, the reusability
 448 of FSK/Al/PTA₃₀ was assessed for five cycles under optimal experimental conditions for HMF
 449 (Fig. 12). After the completion of each reaction, the spent catalyst was separated from the
 450 reaction system by a permanent magnet, thoroughly washed with ethanol, vacuum dried at 110
 451 °C overnight and finally was used for the subsequent runs. The actual amount of catalyst used
 452 in next run was a 3-4% less than the previous run. From the results depicted in Fig. 12 after the
 453 first run the yield of EMF decreased from 93.1% to 85.5%. It is probably a result of partial
 454 leaching of PTA species which have weak electrostatic interaction with the hydroxyl groups
 455 on the surfaces of the FSK/Al support. Nevertheless, the yield of EMF was retained to be
 456 relatively unchanged without noticeable reduction in successive cycles so that after fifth run,
 457 only a 3.3% decrease in efficiency was observed, maybe as a result of deposition of unwashed

458 products on the catalyst and thus covering the catalytic active sites, leading to reduction of
 459 catalytic activity. In table 3, our catalytic system compares favourably in terms of EMF yield,
 460 reaction time and temperature with other systems reported in the literature in which magnetic
 461 and or heteropoly acid-based catalysts have been used.

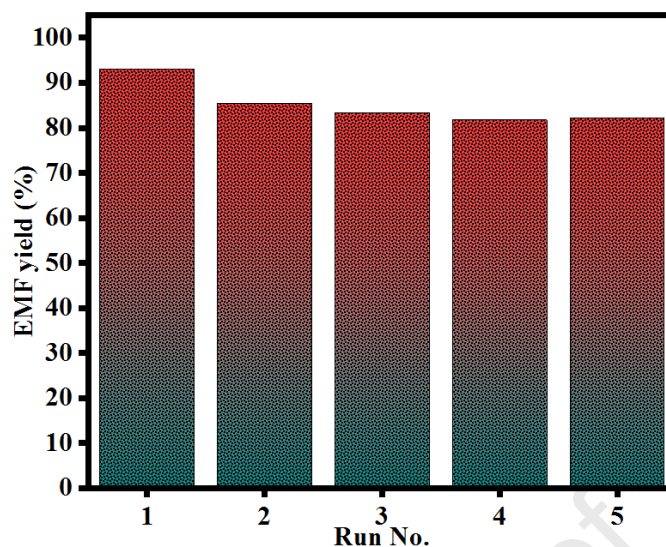
462 Table 3. Comparison of $\text{Fe}_3\text{O}_4@\text{SiO}_2@\text{KCC-1}/\text{Al}/\text{PTA}$ catalyst with other reported magnetic and
 463 heteropoly acid-based catalysts

Entry	Substrate	Catalyst	Temp. (°C)	Time	yield (%)	Reference
1	Fructose	$\text{H}_3\text{PW}_{12}\text{O}_{40}$ Heteropolyacid	130	30 min	76 ^a	[22]
2	HMF	Ta/PTA/SnO ₂	120	45 min	90	[53]
3	Fructose	Phosphotungstic acid	140	130 min	64 ^a	[50]
4	HMF	$\text{H}_4\text{SiW}_{12}\text{O}_{40}/\text{MCM-41}$	90	4 h	77.4	[54]
5	HMF	MCM-41-PTA	100	12 h	90	[24]
6	Fructose	MCM-41-PTA	100	24 h	42.9	[24]
7	Fructose	K-10 clay-HPW (30 wt%)	120	24 h	61.5	[55]
8	HMF	$\text{Fe}_3\text{O}_4@\text{SiO}_2$ -PTA	100	11 h	76.9	[35]
9	HMF	Glu- Fe_3O_4 -SO ₃ H	80	2 h	92	[56]
10	Sucrose	$\text{Fe}_3\text{O}_4@\text{SiO}_2$ -SH-Im- HSO ₄	120	24 h	34.4	[57]
11	Fructose	Magnetic HGC-SO ₃ H	120	24 h	67.4	[58]
12	Fructose	$\text{Fe}_3\text{O}_4@\text{SiO}_2$ - SO ₃ H	100	10	89.3	[34]
13	HMF	$\text{Fe}_3\text{O}_4@\text{C}$ -SO ₃ H	100	12 h	88.4	[36]
14	HMF	$\text{Fe}_3\text{O}_4@\text{SiO}_2@\text{KCC-1}/\text{Al}/\text{PTA}_{30}$	120	1.5 h	93.1	This work
15	Fructose	$\text{Fe}_3\text{O}_4@\text{SiO}_2@\text{KCC-1}/\text{Al}/\text{PTA}_{30}$	120	3 h	62.2	This work

464 ^a Homogeneous catalytic system

465

466



467 Fig. 12. Recyclability of FSK/Al/PTA₃₀ catalyst. Reaction conditions: (HMF: 1 mmol, ethanol: 5 mL,
468 catalyst amount: 60 mg, reaction temperature: 120 °C, reaction time: 1.5 h).
469

470

471 4. Conclusion

472 In summary, in this study, a new method has been developed for the efficient and clean
473 production of EMF through direct etherification of HMF and one-pot conversion of fructose
474 and other carbohydrates over a fibrous mesoporous silica encapsulated magnetic nanospheres.
475 With a simple impregnation, aluminum (10 wt%) can be well incorporated into the shell
476 frameworks to fabricate dendritic mesoporous aluminosilicate microsphere structure. These
477 microspheres were then encapsulated by varying tungstophosphoric acid amount from 10 to 40
478 wt% by impregnation method. The characterization results including SEM and TEM images
479 and EDX illustrated that core shell structures remained intact and still exhibited uniform shape
480 and good monodispersity during synthesis and after functionalization processes with a high
481 dispersion of PTA species throughout the dendritic mesoporous silica shell. The resultant
482 catalysts were efficient for the synthesis of EMF. The catalyst with 30 wt% PTA,
483 FSK/Al/PTA₃₀, showed the highest activity with 99.5% HMF conversion and 93.1% EMF
484 yield, recorded after 1.5 h at 120 °C. While 62.2% of EMF was obtained from fructose at a
485 reaction time of 3 h and at 120 °C. The performance of the catalyst was also evaluated for other
486 carbohydrates under optimized conditions achieved for fructose. The results showed the

487 catalyst is highly efficient in the production of EMF from ketose sugars, whereas not suitable
488 for aldoses. Finally, the reusability of FSK/Al/PTA₃₀ revealed that after four repeat runs, the
489 catalyst was not significantly deactivated, showing a small decrease in EMF yield.

490 **Acknowledgments**

491 The authors wish to acknowledge the support provided by Electricity Supply Board of Ireland
492 (ESB) and the Faculty of Science and Engineering at the University of Limerick for this project.

493 **References**

- 494 [1] H. Hafizi, A. Najafi Chermahini, M. Saraji, G. Mohammadnezhad
495 **The catalytic conversion of fructose into 5-hydroxymethylfurfural over acid**
496 **functionalized KIT-6, an ordered mesoporous silica**
497 Chem. Eng. J., 294 (2016), pp. 380–388, doi.org/10.1016/j.cej.2016.02.082
- 498 [2] C. Thoma, J. Konnerth, W. Sailer-Kronlachner, T. Rosenau, A. Potthast, P. Solt,
499 H.W.G. van Herwijnen
500 **Hydroxymethylfurfural and its derivatives: potential key reactants in adhesives**
501 ChemSusChem, 13 (2020), pp. 5408–5422, doi.org/10.1002/cssc.202001539
- 502 [3] Y. Zhao, K. Lu, H. Xu, L. Zhu, S. Wang
503 **A critical review of recent advances in the production of furfural and 5-**
504 **hydroxymethylfurfural from lignocellulosic biomass through homogeneous**
505 **catalytic hydrothermal conversion**
506 Renew. Sustain. Energy Rev., 139 (2021), pp. 110706,
507 doi.org/10.1016/j.rser.2021.110706

- 508 [4] J. Naja, A. Naja, M. Saraji, A. Shahvar
509 **Dehydration of carbohydrates into 5-hydroxymethylfurfural over vanadyl**
510 **pyrophosphate catalysts**
511 Renew. Energy, 164 (2021), doi.org/10.1016/j.renene.2020.09.022
- 512 [5] L. Gao, Z. Liu, J. Ma, L. Zhong, Z. Song, J. Xu, S. Gan, D. Han, L. Niu
513 **NiSe@NiO_x core-shell nanowires as a non-precious electrocatalyst for upgrading**
514 **5- hydroxymethylfurfural into 2,5-furandicarboxylic acid**
515 Appl. Catal. B Environ. 261 (2020), pp. 118235,
516 doi.org/10.1016/j.apcatb.2019.118235
- 517 [6] G.D. Yadav, R. V. Sharma
518 **Biomass derived chemicals: environmentally benign process for oxidation of 5**
519 **hydroxymethylfurfural to 2,5-diformylfuran by using nano-fibrous Ag-OMS-2-**
520 **catalyst**
521 Appl. Catal. B Environ., 147 (2014), pp. 293–301,
522 doi.org/10.1016/j.apcatb.2013.09.004
- 523 [7] M. Zhang, Z. Li, X. Xin, J. Zhang, Y. Feng, H. Lv
524 **Selective valorization of 5-hydroxymethylfurfural to 2,5-diformylfuran using**
525 **atmospheric O₂ and MAPbBr₃ perovskite under visible light**
526 ACS Catal., 10 (2020), pp. 14793–14800, doi.org/10.1021/acscatal.0c04330
- 527 [8] B. Chen, G. Yan, G. Chen, Y. Feng, X. Zeng, Y. Sun, X. Tang, T. Lei, L. Lin
528 **Recent progress in the development of advanced biofuel 5-ethoxymethylfurfural**

- 529 BMC Energy, 2 (2020), pp. 1–13, doi.org/10.1186/s42500-020-00012-5
- 530 [9] S. Karnjanakom, P. Phanthong, A. Bayu, P. Maneechakr, C. Samart, S. Kongparakul,
531 G. Guan
- 532 **Facile in situ 5-EMF synthesis and extraction processes from catalytic conversion**
533 **of sugar under sustainable long-life cycle**
- 534 ACS Sustain. Chem. Eng., 8 (2020), pp. 14867–14876,
535 doi.org/10.1021/acssuschemeng.0c04517
- 536 [10] X. Liu, R. Wang
- 537 **5-ethoxymethylfurfural-a remarkable biofuel candidate**
- 538 Biomass, Biofuels, Biochem. Recent Adv. Dev. Platf. Chem., (2019), pp. 355–375,
539 doi.org/10.1016/B978-0-444-64307-0.00013-5
- 540 [11] M.I. Alam, S. De, T.S. Khan, M.A. Haider, B. Saha
- 541 **Acid functionalized ionic liquid catalyzed transformation of non-food biomass**
542 **into platform chemical and fuel additive**
- 543 Ind. Crops Prod., 123 (2018), pp. 629–637, doi.org/10.1016/j.indcrop.2018.07.036
- 544 [12] L. di Bitonto, G. Antonopoulou, C. Braguglia, C. Campanale, A. Gallipoli, G.
545 Lyberatos, I. Ntaikou, C. Pastore
- 546 **Lewis-Brønsted acid catalysed ethanolysis of the organic fraction of municipal**
547 **solid waste for efficient production of biofuels**
- 548 Bioresour. Technol., 266 (2018), pp. 297–305, doi.org/10.1016/j.biortech.2018.06.110
- 549 [13] M. Mascal, E.B. Nikitin

- 550 **Direct, high-yield conversion of cellulose into biofuel**
- 551 *Angew. Chemie*, 120 (2008), pp. 8042–8044, doi.org/10.1002/ange.200801594
- 552 [14] F. Yang, J. Tang, R. Ou, Z. Guo, S. Gao, Y. Wang, X. Wang, L. Chen, A. Yuan
- 553 **Fully catalytic upgrading synthesis of 5-ethoxymethylfurfural from biomass-**
- 554 **derived 5-hydroxymethylfurfural over recyclable layered-niobium-molybdate**
- 555 **solid acid**
- 556 *Appl. Catal. B Environ.*, 256 (2019), pp. 117786,
- 557 doi.org/10.1016/j.apcatb.2019.117786
- 558 [15] H. Guo, A. Duereh, Y. Hiraga, T.M. Aida, X. Qi, R.L. Smith
- 559 **Perfect recycle and mechanistic role of hydrogen sulfate ionic liquids as additive**
- 560 **in ethanol for efficient conversion of carbohydrates into 5-ethoxymethylfurfural**
- 561 *Chem. Eng. J.*, 323 (2017), pp. 287–294, doi.org/10.1016/j.cej.2017.04.111
- 562 [16] P. Sudarsanam, R. Zhong, S. Van Den Bosch, S.M. Coman, V.I. Parvulescu, B.F. Sels
- 563 **Functionalised heterogeneous catalysts for sustainable biomass valorisation**
- 564 *Chem. Soc. Rev.*, 47 (2018), pp. 8349–8402, doi.org/10.1039/c8cs00410b
- 565 [17] I. Wheeldon, P. Christopher, H. Blanch
- 566 **Integration of heterogeneous and biochemical catalysis for production of fuels**
- 567 **and chemicals from biomass**
- 568 *Curr. Opin. Biotechnol.*, 45 (2017), pp. 127–135,
- 569 doi.org/10.1016/j.copbio.2017.02.019
- 570 [18] H. Yu, Y. Cao, H. Li, G. Zhao, X. Zhang, S. Cheng

- 571 **An efficient heterogeneous acid catalyst derived from waste ginger straw for**
572 **biodiesel production**
- 573 Renew. Energy, 176 (2021), pp. 533–542, doi.org/10.1016/j.renene.2021.05.098
- 574 [19] S. Alipour, H. Omidvarborna, D.S. Kim
- 575 **A review on synthesis of alkoxymethyl furfural, a biofuel candidate**
- 576 Renew. Sustain. Energy Rev., 71 (2017), pp. 908–926,
577 doi.org/10.1016/j.rser.2016.12.118
- 578 [20] M.A. Hanif, S. Nisar, U. Rashid
- 579 **Supported solid and heteropoly acid catalysts for production of biodiesel**
- 580 Catal. Rev. - Sci. Eng., 59 (2017), pp. 165–188,
581 doi.org/10.1080/01614940.2017.1321452
- 582 [21] O.M. Portilla-Zuñiga, J.J. Martínez, M. Casella, D.I. Lick, Á.G. Sathicq, R. Luque,
583 G.P. Romanelli
- 584 **Etherification of 5-hydroxymethylfurfural using a heteropolyacid supported on a**
585 **silica matrix**
- 586 Mol. Catal., 494 (2020), pp. 111125, doi.org/10.1016/j.mcat.2020.111125
- 587 [22] Y. Yang, M.M. Abu-Omar, C. Hu
- 588 **Heteropolyacid catalyzed conversion of fructose, sucrose, and inulin to 5-**
589 **ethoxymethylfurfural, a liquid biofuel candidate**
- 590 Appl. Energy, 99 (2012), pp. 80–84, doi.org/10.1016/j.apenergy.2012.04.049
- 591 [23] H. Li, K.S. Govind, R. Kotni, S. Shunmugavel, A. Riisager, S. Yang

592 **Direct catalytic transformation of carbohydrates into 5-ethoxymethylfurfural**
593 **with acid-base bifunctional hybrid nanospheres**

594 Energy Convers. Manag., 88 (2014), pp. 1245–1251,
595 doi.org/10.1016/j.enconman.2014.03.037

596 [24] A. Liu, Z. Zhang, Z. Fang, B. Liu, K. Huang

597 **Synthesis of 5-ethoxymethylfurfural from 5-hydroxymethylfurfural and fructose**
598 **in ethanol catalyzed by MCM-41 supported phosphotungstic acid**

599 J. Ind. Eng. Chem., 20 (2014), pp. 1977–1984, doi.org/10.1016/j.jiec.2013.09.020

600 [25] J. Jiao, J. Fu, Y. Wei, Z. Zhao, A. Duan, C. Xu, J. Li, H. Song, P. Zheng, X. Wang, Y.
601 Yang, Y. Liu

602 **Al-modified dendritic mesoporous silica nanospheres-supported nimo catalysts**
603 **for the hydrodesulfurization of dibenzothiophene: efficient accessibility of active**
604 **sites and suitable metal–support interaction**

605 J. Catal., 356 (2017), pp. 269–282, doi.org/10.1016/j.jcat.2017.10.003

606 [26] M.D. Marquez-Medina, S. Mhadmhan, A.M. Balu, A.A. Romero, R. Luque

607 **Post-synthetic mechanochemical incorporation of Al-species into the framework**
608 **of porous materials: toward more sustainable redox chemistries**

609 ACS Sustain. Chem. Eng., 7 (2019), pp. 9537–9543,
610 doi.org/10.1021/acssuschemeng.9b00912

611 [27] H. Atia, U. Armbruster, A. Martin

612 **Dehydration of glycerol in gas phase using heteropolyacid catalysts as active**
613 **compounds**

- 614 J. Catal., 258 (2008), pp. 71–82, doi.org/10.1016/j.jcat.2008.05.027
- 615 [28] K. Usha Nandhini, J. Herbert Mabel, B. Arabindoo, M. Palanichamy, V. Murugesan
- 616 **The influence of phosphotungstic acid acidity on Al-MCM-41 in t-butylation of**
- 617 **phenol with t-butyl alcohol**
- 618 Microporous Mesoporous Mater., 96 (2006), pp. 21–28,
- 619 doi.org/10.1016/J.MICROMESO.2006.06.015
- 620 [29] B. Liu, Z. Zhang
- 621 **Catalytic conversion of biomass into chemicals and fuels over magnetic catalysts**
- 622 ACS Catal., 6 (2016), pp. 326–338, doi.org/10.1021/acscatal.5b02094
- 623 [30] R.V. Quah, Y.H. Tan, N.M. Mubarak, M. Khalid, E.C. Abdullah, C. Nolasco-Hipolito
- 624 **An overview of biodiesel production using recyclable biomass and non-biomass**
- 625 **derived magnetic catalysts**
- 626 J. Environ. Chem. Eng., 7 (2019), pp. 103219, doi.org/10.1016/j.jece.2019.103219
- 627 [31] A.P. Ingle, R.R. Philippini, S. Silvério da Silva
- 628 **Pretreatment of sugarcane bagasse using two different acid-functionalized**
- 629 **magnetic nanoparticles: a novel approach for high sugar recovery**
- 630 Renew. Energy, 150 (2020), pp. 957–964, doi.org/10.1016/j.renene.2019.11.146
- 631 [32] M.B. Gawande, Y. Monga, R. Zboril, R.K. Sharma
- 632 **Silica-decorated magnetic nanocomposites for catalytic applications**
- 633 Coord. Chem. Rev., 288 (2015), pp. 118–143, doi.org/10.1016/j.ccr.2015.01.001
- 634 [33] W. Xie, H. Wang

- 635 **Immobilized polymeric sulfonated ionic liquid on core-shell structured**
636 **Fe₃O₄/SiO₂ composites: a magnetically recyclable catalyst for simultaneous**
637 **transesterification and esterifications of low-cost oils to biodiesel**
638 *Renew. Energy*, 145 (2020), pp. 1709–1719, doi.org/10.1016/j.renene.2019.07.092
- 639 [34] Z. Zhang, Y. Wang, Z. Fang, B. Liu
- 640 **Synthesis of 5-ethoxymethylfurfural from fructose and inulin catalyzed by a**
641 **magnetically recoverable acid catalyst**
642 *Chempluschem*, 79 (2014), pp. 233–240, doi.org/10.1002/cplu.201300301
- 643 [35] J.L.L. S.G. Wang, Z.H. Zhang, B. Liu
- 644 **Silica coated magnetic Fe₃O₄ nanoparticles supported phosphotungstic acid: a**
645 **novel environment-friendly catalyst for the synthesis of 5-ethoxymethylfurfural**
646 **from 5-hydroxymethylfurfural and fructose**
647 *Catal. Sci. Technol.*, 3 (2013), pp. 2104–2112,
648 doi.org/https://doi.org/10.1039/C3CY00223C
- 649 [36] Z. Yuan, Z. Zhang, J. Zheng, J. Lin
- 650 **Efficient synthesis of promising liquid fuels 5-ethoxymethylfurfural from**
651 **carbohydrates**
652 *Fuel*, 150 (2015), pp. 236–242, doi.org/10.1016/j.fuel.2015.02.020
- 653 [37] V. Polshettiwar, D. Cha, X. Zhang, J.M. Basset
- 654 **High-surface-area silica nanospheres (KCC-1) with a fibrous morphology**
655 *Angew. Chemie - Int. Ed.*, 49 (2010), pp. 9652–9656, doi.org/10.1002/anie.201003451

- 656 [38] K. Yu, X. Zhang, H. Tong, X. Yan, S. Liu
657 **Synthesis of fibrous monodisperse core-shell Fe₃O₄/SiO₂/KCC-1**
658 Mater. Lett., 106 (2013), pp. 151–154, doi.org/10.1016/j.matlet.2013.04.112
- 659 [39] Z. Sun, H. Li, D. Guo, J. Sun, G. Cui, Y. Liu, Y. Tian, S. Yan
660 **A multifunctional magnetic core-shell fibrous silica sensing probe for highly**
661 **sensitive detection and removal of Zn²⁺ from aqueous solution**
662 J. Mater. Chem. C, 3 (2015), pp. 4713–4722, doi.org/10.1039/c5tc00166h
- 663 [40] Y. Wang, X. Du, Z. Liu, S. Shi, H. Lv
664 **Dendritic fibrous nano-particles (DFNPs): rising stars of mesoporous materials**
665 J. Mater. Chem. A, 7 (2019), pp. 5111–5152, doi.org/10.1039/c8ta09815h
- 666 [41] H. Deng, X. Li, Q. Peng, X. Wang, J. Chen, Y. Li
667 **Monodisperse magnetic single-crystal ferrite microspheres**
668 Angew. Chemie, 117 (2005), pp. 2842–2845, doi.org/10.1002/ange.200462551
- 669 [42] J. Yang, D. Shen, Y. Wei, W. Li, F. Zhang, B. Kong, S. Zhang, W. Teng, J. Fan, W.
670 Zhang, S. Dou, D. Zhao
671 **Monodisperse core-shell structured magnetic mesoporous aluminosilicate**
672 **nanospheres with large dendritic mesochannels**
673 Nano Res., 8 (2015), pp. 2503–2514, doi.org/10.1007/s12274-015-0758-2
- 674 [43] S.M. Yusof, R. Othaman, H.D. Setiabudi, L.P. Teh
675 **Modified fibrous silica for enhanced carbon dioxide adsorption: role of metal**
676 **oxides on physicochemical properties and adsorption performance**

- 677 J. Solid State Chem., 294 (2021), pp. 121845, doi.org/10.1016/j.jssc.2020.121845
- 678 [44] L. Li, S. Yu, F. Liu, J. Yang, S. Zhaug
- 679 **Reactions of turpentine using Zr-MCM-41 family mesoporous molecular sieves**
- 680 Catal. Letters, 100 (2005), pp. 227-233, doi.org/10.1007/s10562-005-3460-2
- 681 [45] E.P. Parry
- 682 **An infrared study of pyridine adsorbed on acidic solids. Characterization of**
- 683 **surface acidity**
- 684 J Catal., 2 (5) (1963), pp. 371-379, doi.org/10.1016/0021-9517
- 685 [46] B.B. Bardin, S. V. Bordawekar, M. Neurock, R.J. Davis
- 686 **Acidity of Keggin-type heteropolycompounds evaluated by catalytic probe**
- 687 **reactions, sorption microcalorimetry, and density functional quantum chemical**
- 688 **calculations**
- 689 J. Phys. Chem. B, 102 (1998), pp. 10817–10825, doi.org/10.1021/jp982345y
- 690 [47] P.Y. Hoo, A.Z. Abdullah
- 691 **Direct synthesis of mesoporous 12-tungstophosphoric acid sba-15 catalyst for**
- 692 **selective esterification of glycerol and lauric acid to monolaurate**
- 693 Chem. Eng. J., 250 (2014), pp. 274–287, doi.org/10.1016/j.cej.2014.04.016
- 694 [48] R. Rocchicciolidelcheff, C.; Fournier, M.; Franck, R.; Thouvenot
- 695 **Vibrational investigations of polyoxometalates. 2. evidence for anion-anion**
- 696 **interactions in molybdenum (VI) and tungsten (VI) compounds related to the**
- 697 **Keggin structure**

- 698 Inorg. Chem., (1983), pp. 207–216, doi.org/10.1021/ic00144a006
- 699 [49] S.K.R. Patil, C.R.F. Lund
- 700 **Formation and growth of humins via aldol addition and condensation during**
- 701 **acid-catalyzed conversion of 5-hydroxymethylfurfural**
- 702 Energy & Fuels, 25 (2011), pp. 4745–4755, doi.org/10.1021/ef2010157
- 703 [50] H. Guo, X. Qi, Y. Hiraga, T.M. Aida, R.L. Smith
- 704 **Efficient conversion of fructose into 5-ethoxymethylfurfural with hydrogen**
- 705 **sulfate ionic liquids as co-solvent and catalyst**
- 706 Chem. Eng. J., 314 (2017), pp. 508–514, doi.org/10.1016/j.cej.2016.12.008
- 707 [51] C.M. Lew, N. Rajabbeigi, M. Tsapatsis
- 708 **One-pot synthesis of 5-(ethoxymethyl)furfural from glucose using Sn-BEA and**
- 709 **Amberlyst catalysts**
- 710 Ind. Eng. Chem. Res., 51 (2012), pp. 5364–5366, doi.org/10.1021/ie2025536
- 711 [52] B. Liu, Z. Zhang
- 712 **One-pot conversion of carbohydrates into 5-ethoxymethylfurfural and ethyl d-**
- 713 **glucopyranoside in ethanol catalyzed by a silica supported sulfonic acid catalyst**
- 714 RSC Adv., 3 (2013), pp. 12313–12319, doi.org/10.1039/c3ra41043a
- 715 [53] P.K. Kumari, B.S. Rao, D. Padmakar, N. Pasha, N. Lingaiah
- 716 **Lewis acidity induced heteropoly tungstate catalysts for the synthesis of 5-**
- 717 **ethoxymethyl furfural from fructose and 5-hydroxymethylfurfural**
- 718 Mol. Catal., 448 (2018), pp. 108–115, doi.org/10.1016/j.mcat.2018.01.034

- 719 [54] P. Che, F. Lu, J. Zhang, Y. Huang, X. Nie, J. Gao, J. Xu
720 **Catalytic selective etherification of hydroxyl groups in 5-hydroxymethylfurfural**
721 **over H₄SiW₁₂O₄₀/MCM-41 nanospheres for liquid fuel production**
722 *Bioresour. Technol.*, 119 (2012), pp. 433–436, doi.org/10.1016/j.biortech.2012.06.001
- 723 [55] A. Liu, B. Liu, Y. Wang, R. Ren, Z. Zhang
724 **Efficient one-pot synthesis of 5-ethoxymethylfurfural from fructose catalyzed by**
725 **heteropolyacid supported on K-10 clay**
726 *Fuel*, 117 (2014), pp. 68–73, doi.org/10.1016/j.fuel.2013.09.072
- 727 [56] R.S. Thombal, V.H. Jadhav
728 **Application of glucose derived magnetic solid acid for etherification of 5-HMF to**
729 **5-EMF, dehydration of sorbitol to isosorbide, and esterification of fatty acids**
730 *Tetrahedron Lett.*, 57 (2016), pp. 4398–4400, doi.org/10.1016/j.tetlet.2016.08.061
- 731 [57] S. Yin, J. Sun, B. Liu, Z. Zhang
732 **Magnetic material grafted cross-linked imidazolium based polyionic liquids: an**
733 **efficient acid catalyst for the synthesis of promising liquid fuel 5-**
734 **ethoxymethylfurfural from carbohydrates**
735 *J. Mater. Chem. A*, 3 (2015), pp. 4992–4999, doi.org/10.1039/c4ta06135g
- 736 [58] Y.Y. Bai, S. Su, S. Wang, B. Wang, R.C. Sun, G. Song, L.P. Xiao
737 **Catalytic conversion of carbohydrates into 5-ethoxymethylfurfural by a magnetic**
738 **solid acid using γ -valerolactone as a co-solvent**
739 *Energy Technol.*, 6 (2018), pp. 1951–1958, doi.org/10.1002/ente.201800090

Declaration of interests

- The authors declare that they have no known competing financial interests or personal relationships that could have appeared to influence the work reported in this paper.
- The authors declare the following financial interests/personal relationships which may be considered as potential competing interests:

Journal Pre-proof